Morphology dependent resonance modes in highly porous TiO_2 microspheres

Imon Kalyan, and C. V. Krishnamurthy

Citation: Journal of Applied Physics **124**, 133102 (2018); doi: 10.1063/1.5046488
View online: https://doi.org/10.1063/1.5046488
View Table of Contents: http://aip.scitation.org/toc/jap/124/13
Published by the American Institute of Physics

Morphology dependent resonance modes in highly porous TiO_2 microspheres

Imon Kalyan[a)] and C. V. Krishnamurthy
Department of Physics, Indian Institute of Technology Madras, Chennai, Tamilnadu 600036, India

(Received 28 June 2018; accepted 10 September 2018; published online 3 October 2018)

Micro and nano structures of titanium dioxide (TiO_2) are well-known for their photocatalytic application. High surface area and high light scattering efficiency in such structures enhance their photocatalytic activity. The present work explores the possibility of enhancing photocatalytic activity through mesoporous TiO_2 spheres by exploiting the coexistence of high porosity and morphology dependent resonance (MDR) modes. A controlled synthesis of TiO_2 spheres with nano-crystalline grains of anatase phase and high surface area of about 96 m^2/g has been successfully accomplished leading to mesoporous particles with uniformly distributed pores of small diameters much less than the wavelength of incident light. Despite the high porosity, MDR modes are observed in the photoluminescence spectrum of a single sphere. As inclusion of pores may produce significant changes in the refractive index (RI) of the resonator, and as the quality and density of the modes depend on the RI of the resonator, it is important to have a procedure to determine the RI of the resonator as well as to characterize the MDR modes. An iterative procedure that is quite general is presented for mode identification and for the determination of the porosity-induced reduction in the RI and for ascertaining the presence of chromatic dispersion. The presence of high surface area as well as of MDR modes of reasonably high Q-factor makes these particles promising for photo electrochemical applications. *Published by AIP Publishing.* https://doi.org/10.1063/1.5046488

I. INTRODUCTION

Morphology dependent resonance (MDR) modes are the resonance modes of high quality (Q) factor in a micro-cavity occurring due to the trapping of light caused by total internal reflection at its boundary. These modes are also referred to in the literature as whispering gallery modes (WGM).[1] The presence of such resonances enhances the interaction of light with the intrinsic material mostly near the surface of the sphere.[1] Spectral positions of these modes are sensitive to the morphology of the sphere and the difference between the refractive indices of the resonator and surrounding medium. MDR modes have been attracting interest due to their various applications in fields like lasing, sensing, light trapping, nonlinear photonics, etc.[2–4]

Microparticles of TiO_2 in the form of disk,[5] sphere,[6] etc. have been studied as micro cavity resonators due to their various desirable properties like high ultraviolet (UV) light absorption and high scattering of visible and near infrared light, CMOS compatibility,[5] thermal and chemical stability, biocompatibility,[7] etc. Spherical resonators are attractive because of their simplicity of production and capability of producing modes with highest quality factor as compared to resonators with other shapes. TiO_2 being a photocatalytic material in the presence of MDR modes highly enhances the light matter interaction and hence its photocatalytic activity. Paunoiu *et al.*[6] have shown the presence of MDR modes in TiO_2 microspheres and suggested their usefulness in photocatalysis. Das *et al.*[8] have shown that the presence of MDR mode in mesoporous TiO_2 enhances the efficiency of dye sensitized solar cells.

TiO_2 is well known for its photocatalytic applications. During photocatalytic reaction, light induced charges of the TiO_2 particle take part in redox reaction with the molecules or atoms adsorbed on its surface.[9] The presence of high surface area enhances the interaction of TiO_2 with the external molecules to be catalyzed. The presence of MDR modes enhances its scattering efficiency and hence its light harvesting capability. The presence of both high surface area and MDR modes makes these particles more promising for photo electro chemical applications. The quality of scattering by a resonator is defined by its Q-factor and free spectral range (FSR) which are dependent on the morphology and RI of the resonator. A high Q-factor or low loss resonator requires a homogeneous, non-absorbing medium with a smooth surface.[1] Introduction of pores as inclusion inside the sphere may cause inhomogeneity, rough surface, and change in the effective RI from its bulk RI.[10] Size and distribution of the pores need to be controlled to retain the MDR modes in a resonator with high surface area, and a correct estimation of RI is necessary to have an understanding and control over the quality of light scattering by the particles. Direct methods of the estimation of RI from an unknown material are non-trivial. However, various approximation and iterative methods have been proposed for the estimation of RI via identification of the MDR modes. Paunoiu *et al.*[6] have found that RI from the MDR modes occurred in the photoluminescence (PL) spectrum of TiO_2 microsphere considering it to be constant in the range of observation. In their work, RI is estimated by adjusting the size and RI simultaneously to minimize the difference between calculated and observed mode positions. Ikari *et al.*[11] have identified the modes of Eu^{3+} doped TiO_2 by varying the estimation of size and RI and matching the mode positions of experimental and simulated

[a)]Email: kalyanimon1@gmail.com.

spectrum. However, the dispersion of the RI was considered to be linear in this case. This method is suitable over a small range of wavelength (WL) where RI has linear and lesser dispersion. Moirangthem *et al.*[12] have also introduced a method of finding RI of ZnO micro sphere where the dispersion characteristics of bulk ZnO are assumed to be applicable for the ZnO microsphere as well. However, the presence of pores or impurities may cause higher order changes in the dispersion of RI from its bulk value.

In most of the iterative methods, RI and size of the sphere are varied iteratively to minimize the separations between theoretical and experimental modes. An MDR mode is defined by an integer number known as angular mode number (l) which is dependent on the size parameter and RI of the sphere. Estimation of the value of l iteratively involves comparatively fewer steps.

In this work, mesoporous TiO_2 microspheres with a very high surface area of about 96 m^2/g are synthesized. Such high surface area was obtained due to the use of an organic structure directing reagent. The sol-gel method was used to obtain inorganic-organic hybrid amorphous spheres. When solvothermally treated, amorphous hybrid TiO_2 micro spheres convert to mesoporous TiO_2 microspheres of high surface area consisting of nanocrystals and nanopores due to the removal of the structure directing agent. Due to the uniform distribution of the structure directing agent in the amorphous sphere, pores generated during hydrothermal process also remains uniformly distributed without disturbing the spherical morphology of the sphere. X-ray diffraction (XRD), Raman spectrum, and Brunauer–Emmett–Teller (BET) surface area measurements have been done to confirm the crystalline and porous nature of the synthesized particles. Scanning electron microscope (SEM) images are obtained to study the morphology of the material. MDR modes were observed in the PL spectrum of a single sphere. MDR modes observed could not be explained by the RI of bulk TiO_2 as its effective RI and its dispersion got changed from its bulk value due to high porosity. An iterative procedure that is quite general and easy to follow is presented for mode identification which leads to the extraction of RI. This method does not require prior knowledge of RI of the medium in the bulk. RI is extracted at each TE mode, and dispersion in RI is obtained by fitting the Sellmeier equation to the extracted data. By identifying the MDR modes in the PL spectrum of the microspheres correctly, the real part of the RI of the spheres is estimated and found to be much smaller than that of bulk anatase.

II. EXPERIMENTAL INVESTIGATIONS

A. Sample preparation

Amorphous precursor microspheres were synthesized by hydrolysis of titanium isopropoxide (TTIP) in n-butanol in the presence of hexadecylamine (HDA) as structure directing agent using the sol-gel process, as mentioned in the work of Cao *et al.*[13] TTIP (97%) and HDA (90%) were purchased from Sigma-Aldrich. For the synthesis of amorphous precursor microspheres, 1.987 g of HDA was dissolved in 100 mL of n-butanol (Rankem) followed by the addition of 0.7 mL of 0.1M aqueous potassium chloride (AR, Merck) solution. 2.2 mL of TTIP was added to this solution and stirred at a temperature around 20 °C. The solution became milky white within 15 min. This white solution was kept static at room temperature for 18 h to obtain precursor microspheres of size in the range of 2–5 μm. The precursor spheres were collected via centrifugation and cleaned with n-butanol once followed by cleaning with ethanol for three times. The clean spheres were dried at room temperature for a day in air. 1 g of the dried powder was dispersed in a mixture of 20 mL ethanol and 10 mL water and underwent solvothermal treatment at 160 °C for 20 h in a Teflon lined autoclave of 50 mL capacity.

During the sol-gel process, amino group of HDA is hydrogen bonded to the amorphous TiO_2 produced from hydrolysis of TTIP to form an inorganic-organic hybrid composite. With time, this composite condenses to a denser form and takes a spherical shape to minimize surface free energy.[14] During the solvothermal process, amorphous TiO_2 nanoparticles change their phase to anatase crystals and also grow in size along with the HDA slowly getting removed leaving pores in TiO_2 domain. Solvothermal treatment for smaller time intervals resulted in spheres with lesser porosity. Longer time intervals appear to lead to loose packing of the nano-crystallites.[13]

For the PL measurement, a low concentration dispersion of the above particles in ethanol was obtained and drop-casted on a silicon substrate and dried at room temperature over a night. A heat treatment at 150 °C for 5 h was done on these spheres to remove any remaining organic compound on it. For XRD and porosity measurement, the solvothermally treated spheres were dried for a day to obtain in powder form and then underwent a heat treatment at 150 °C for 5 h, along with the drop-casted spheres.

B. Sample characterization

Crystallinity of the material was analyzed from the XRD pattern using a Bruker D8 Discover diffractometer (Cu-Kα source). Raman spectrum and PL-spectrum of a single particle were obtained by exciting a single particle with a laser light of WL 488 nm, using a HORIBA JOBIN VYON HR 800 UV Raman spectrometer. BET surface area and porosity measurements were carried out using a Micromeritics ASAP2020 analyzer. Energy dispersive x-ray (EDX) analysis of the synthesized material was done with a scanning electron microscope (FEG Quanta 400 FESEM). Images of the single spheres and their surfaces were studied with high resolution SEM (Hitachi S4800 HR-SEM).

Peaks corresponding to anatase TiO_2 appeared in the XRD pattern of the sample as shown in Fig. 1(a). Average crystal sizes of the particles calculated using Scherrer formula is 7 nm. Figure 1(b) represents the Raman spectrum obtained by focusing a laser beam of WL 488 nm on a single sphere. Peaks at 143.9 (E_g), 198.3 (E_g), 399.3(B_{1g}), 522.8 (A_{1g} and B_{1g}), and 642.1 (E_g) in the Raman spectrum confirm its phase to be anatase.[15] The SEM image of the corresponding single sphere can be seen in the inset of Fig. 1(b). However, EDX analysis on a single sphere (Fig. 2) of the sample indicates the presence of carbon and nitrogen

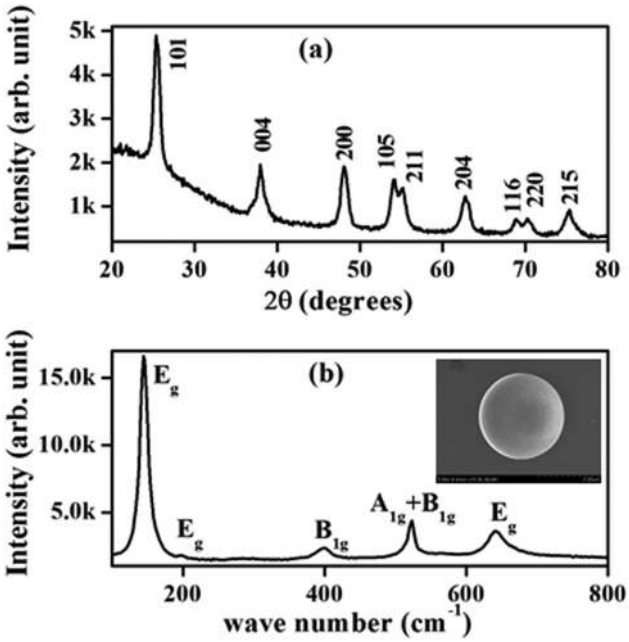

FIG. 1. (a) XRD of the powder sample; (b) Raman spectrum of a single microsphere and corresponding SEM image in the inset.

as well. The peak representing silicon in the EDX data is due to the contribution from the substrate.

Mesoporosity of the spheres is confirmed by BET surface area and porosity measurement using nitrogen adsorption desorption isotherms at 77 K. BET surface area was measured to be 96.0 m^2/g. Adsorption and desorption isotherms are shown in Fig. 3(a) by black solid curves and a red dashed curve, respectively. Hysteresis observed in the adsorption desorption isotherm indicates the material to be of type IV according to the IUPAC classification.[16] The corresponding Barrett-Joyner-Halenda (BJH) calculation for pore size distribution is shown in Fig. 3(b). In Fig. 3(b), differential adsorption volume as a function of pore width is plotted for desorption isotherm. Sizes of the pores are found to be around 7.6 nm. A mesoporous surface can be observed in the high resolution SEM image in the inset of Fig. 3(b).

C. MDR modes in PL spectrum

PL of an isolated single microsphere is obtained by a micro Raman spectrometer. Since excitation energy (2.54 eV) is much below the band gap (3.2 eV) of pure anatase TiO_2, luminescence observed in the visible spectrum may be attributed to the inter-band transitions from the defect states due to oxygen-vacancies[6,17,18] or due to the presence of N and C.[19,20] PL is measured in a range of WL much away from the Raman lines of anatase TiO_2. MDR modes are observed on the top of the wide PL spectrum.

It has been shown recently that spheres of birefringent media lead to split modes.[21] It has also been shown that MDR modes of polycrystalline TiO_2 (anatase phase) spheres made of birefringent grains resemble those of an equivalent isotropic Mie sphere, when the grain size is much small compared to the WL of light responsible for the generation of the modes.[21] The mode features observed in the spectrum shown

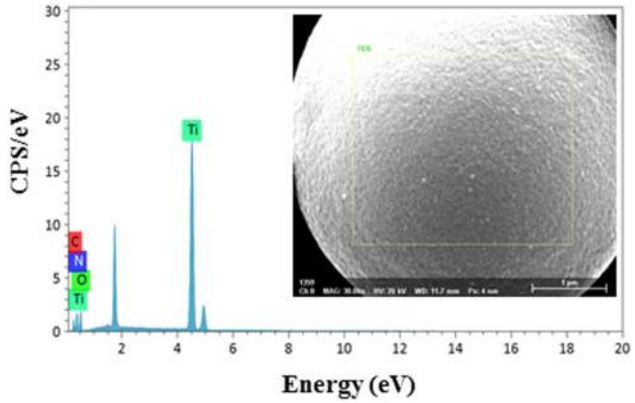

FIG. 2. EDX spectrum of a single microsphere.

in Fig. 4(a) do not indicate mode splitting, suggesting that the mesoporous sphere may be effectively isotropic in nature. However, the presence of high porosity is expected to lower the RI and may lead to changes in the dispersion of RI influencing the mode positions and Q-factors. As the observed sizes of the grains (~7 nm) and of the pores (~7.6 nm) of the mesoporous sphere are very small compared to the visible WL, the mesoporous sphere has been considered to be an effective homogeneous and isotropic sphere. Accordingly, Mie theory has been employed for the identification of the modes. Figure 4(a) shows the MDR modes observed in the emission spectrum for the spheres with diameters 4.32 μm, 3.18 μm, and 2.91 μm, respectively. The corresponding SEM images for the spheres with diameters 4.32 μm, 3.18 μm, and 2.91 μm are shown in Fig. 4(b). Experimental spectrum is denoted by a black curve in Fig. 4(a), and the simulated efficiency spectrum with the corrected RI is shown by the red curve in the same figure. Mode identifications for 3.18 μm

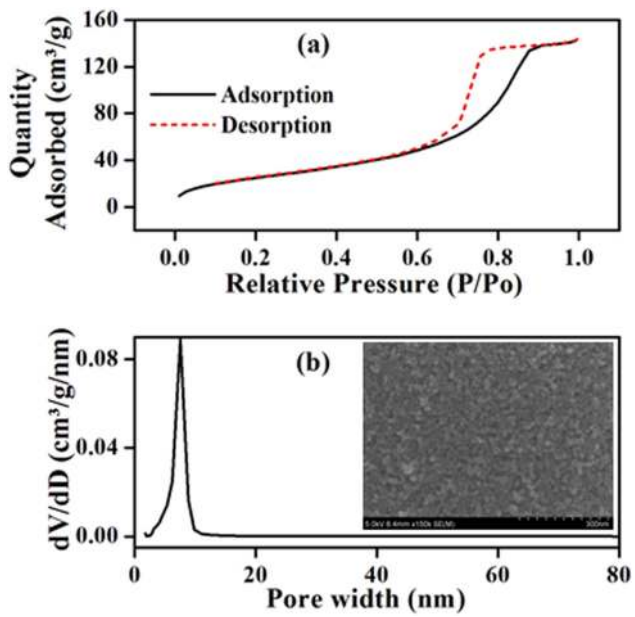

FIG. 3. (a) Nitrogen adsorption and desorption isotherms are represented by black (solid) and red (dashed) curves, respectively; (b) Differential pore volume vs pore width from BJH calculation. A high resolution SEM image of the surface of a sphere is shown in the inset of (b)

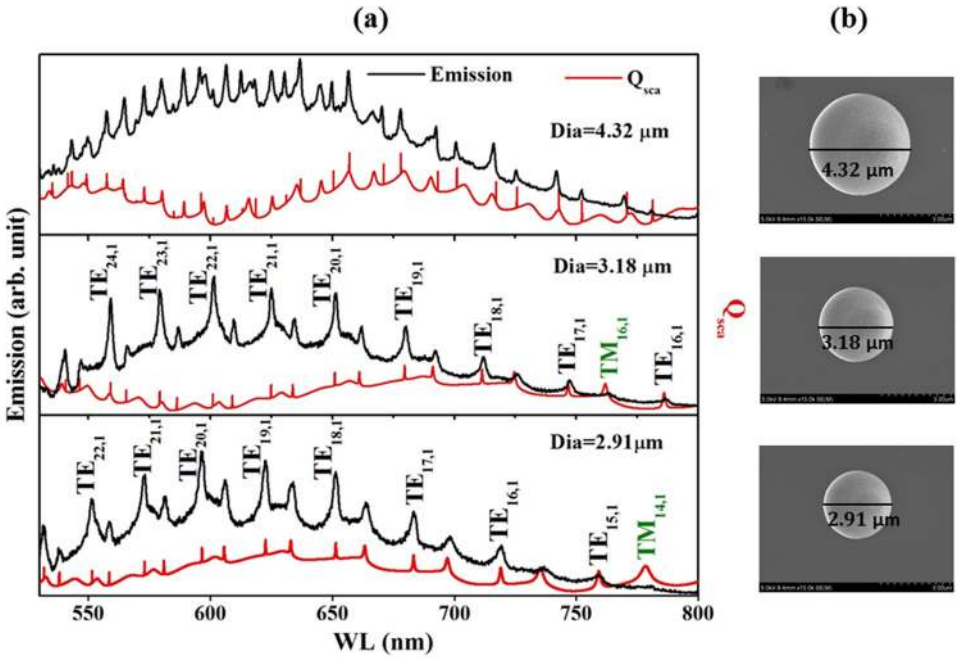

FIG. 4. (a) MDR modes on the micro PL spectrum of a single sphere are shown in black (upper plot), and the corresponding scattering efficiency spectrum obtained using Mie theory with extracted RI is shown by the red curve (lower plot) for spheres with diameters 4.32 μm, 3.18 μm, and 2.91 μm. Identification of all the TE modes observed is indicated over the corresponding modes. TM modes alternate with TE modes. Only one TM mode corresponding to the smallest l is shown to avoid cluttering. (b) SEM images of the spheres corresponding to the MDR spectra of spheres with diameters 4.32 μm, 3.18 μm, and 2.91 μm.

and 2.91 μm particles are shown in Fig. 4(a). Due to its bigger diameter, modes corresponding to 4.32 μm have higher spectral density. Mode identification of 4.32 μm sphere in Fig. 4(a) is shown in Fig. 7.

The method followed for the assignment of mode numbers and extraction of RI is discussed in detail in the Sec. III.

III. ANALYSIS OF THE MDR MODES

A. Mode identification and RI extraction procedure

1. Theory of MDR modes

When the circumference of a spherical particle is an integral multiple of the WL of light inside the sphere, the light entering the sphere can get trapped inside the sphere due to total internal reflection producing standing waves inside the sphere mostly near its surface. This leads to MDR modes. From a ray optics point of view, one can argue these modes to appear in a dielectric sphere of refractive index (RI) n and radius a, when light of particular WL, λ_l satisfies Eq. (1).

$$\frac{2\pi a}{\lambda_l/n(\lambda_l)} = l, \tag{1}$$

However, Eq. (1) is a geometrical optics aspect and is more convincing when $l \to \infty$. In general, the interaction of light with spherical particles can be explained by Mie theory, by solving vector wave equations in spherical polar coordinates, applying boundary conditions. Scattering cross section (C_{sca}) and scattering efficiency [$Q_{sca} = C_{sca}/(\pi a^2)$] for a homogeneous, isotropic, nonmagnetic, perfect sphere can be calculated from the Mie–Debye theory[22] as given in Eq. (2):

$$Q_{sca} = \frac{2}{x^2}\sum_{l=1}^{l=\infty}(2l+1)(|a_l|^2 + |b_l|^2), \tag{2}$$

$$a_l = \frac{n^2 j_l(nx)[x j_l(x)]' - j_l(x)[nx\, j_l(nx)]'}{n^2 j_l(nx)[x h_l^1(x)]' - h_l^1(x)[nx\, j_l(nx)]'}, \tag{3a}$$

$$b_l = \frac{j_l(nx)[x j_l(x)]' - j_l(x)[nx\, j_l(nx)]'}{j_l(nx)[x h_l^1(x)]' - h_l^1(x)[nx\, j_l(nx)]'}, \tag{3b}$$

where j_l and h_l^1 are spherical Bessel and spherical Hankel function of first kind, respectively, $x = 2\pi a/\lambda$. a_l and b_l are the scattering coefficients which are functions of a, λ, and n. MDR modes appear in the scattering spectrum of a sphere when the denominators of a_l and b_l vanish. The line shape of $|a_l^2|$ and $|b_l^2|$ in the vicinity of a resonance is characterized by a Fano profile.[23] For larger values of l, this line shape tends to take a Lorentzian profile. When the denominator of b_l (a_l) vanishes, alignment of electric (magnetic) field becomes transverse to the radial direction and modes are called TE (TM) modes. In the domain of $1 << x < l$, the function in the denominator of b_l in Eq. (3a), denoted by ϕ_l, can be simplified in terms of Bessel function (j_l) and Neumann function (y_l).[24] The modes are determined by the zeroes of ϕ_l as indicated by Eq. (4).

$$\phi_l(x, n) = n y_l(x) j_l'(nx) - y_l'(x) j_l(nx) = 0. \tag{4}$$

MDR observed in the emission spectrum are analogous to that observed in the scattering spectrum.[1] MDR modes are characterized by four parameters: polarization (TE/TM), angular momentum mode number (l), radial mode number (ρ), and azimuthal mode number (m). l and ρ characterize the number of intensity maxima along the great perimeter of the sphere and along the radial direction of the sphere, respectively. For a particular value of l, there exists $2l+1$ number of modes corresponding to different values of m in the range of $-l$ to $+l$. For a perfect homogeneous sphere, spectral positions of the modes are independent of m, and there exists $2l+1$ fold degeneracy for a particular value of l. However,

deviation from ideal conditions of a sphere due to deformation in the spherical shape,[25] presence of inclusions,[26] birefringence of the constituting material,[27] etc. may lead to lifting of degeneracy.

When radius is considered to be constant, ϕ_l is a function of only λ and n alone. Equation (4) may have several solutions for a fixed value of l when calculated as a function of λ or n, as shown in Figs. 5(a) and 5(b) respectively. Each solution is indicated by a radial mode number ρ. The first three solutions of $\phi(\lambda, n) = 0$ corresponds to $\rho = 1$, 2, and 3, which can be seen in Figs. 5(a) and 5(b), indicated by green, blue, and red colored points, respectively. In Fig. 5(a), $\phi_l(\lambda)$ vs λ plot for $l = 30$ (indicated by the solid line) and $l = 31$ (indicated by the dashed line) are shown for a constant value of a and n. Modes with higher values of l correspond to lower WL (higher energy). For a particular value of l, the solution with the longest value of WL (lowest energy) corresponds to the smallest value of radial mode number ($\rho = 1$). It can also be observed that differences of the spectral position of two neighboring modes corresponding to two l values with different values of ρ are different. Figure 5(b) shows $\phi_l(n)$ vs n plot for $l = 30$ (indicated by the solid line) and $l = 31$(indicated by the dashed line) for a fixed value of x. For a fixed value of ρ, solutions of n corresponding to a higher value of l are of greater value. For a fixed value of l, RI corresponding to higher values of ρ is higher. The calculation has been done without considering the imaginary part of the RI. Introduction of the imaginary part does not change the mode positions but reduces the Q-factors of the modes.

Modes with different polarizations and radial mode numbers can be distinguished from the separation between two neighboring modes or FSR. Lam *et al.*[24] have shown analytically that the difference in the size parameters ($\Delta x_l^{FSR} = x_l - x_{l-1}$) of two neighboring modes of same polarization and same radial mode number is related to n by a series of $(l + 0.5)^{-1/3}$. Zeroth order approximation of FSR in WL domain implies that $\Delta\lambda_l^{FSR}$ is proportional to λ^2. However, the slope of $\Delta\lambda_l^{FSR}$ vs λ^2 plot for modes belonging to different values of ρ and different polarizations differs due to corresponding multipliers of the higher orders of $(l + 0.5)^{-1/3}$. $\Delta\lambda_l^{FSR}$ vs λ^2 plot for TE modes with $\rho = 1$ and $\rho = 2$ are shown in Fig. 6.

The efficiency of the MDR modes to confine light inside the cavity is quantified by its Q-factor. The Q-factor is defined as Eq. (5).

$$Q = \frac{\omega_o}{\Delta\omega_{FWHM}}, \tag{5}$$

where ω_o is the angular frequency of the resonance and $\Delta\omega_{FWHM}$ is the full width at half maximum (FWHM) of the resonance peak in angular frequency domain. $\Delta\omega_{FWHM}$ is dependent on l and ρ.

2. Method of assignment of the mode number to the MDR modes

Mode identification is done from the relation of x, n, and l as given in Eq. (4). x at the modes is obtained from the size extracted from the SEM image, and the spectral positions of the modes are obtained from the measured spectrum. RI of the synthesized sphere differs from that of bulk RI[28] due to its porous nature. Other factors like nano crystalline sizes of the grains[29] and the presence of impure elements[11] may contribute to the change in RI as well. If the value of either l or n is known, the other can be calculated using Eq. (4). In our method, firstly modes of the same polarization and radial mode number are grouped from the knowledge of their FSR. An educative guess of l can be obtained from the first

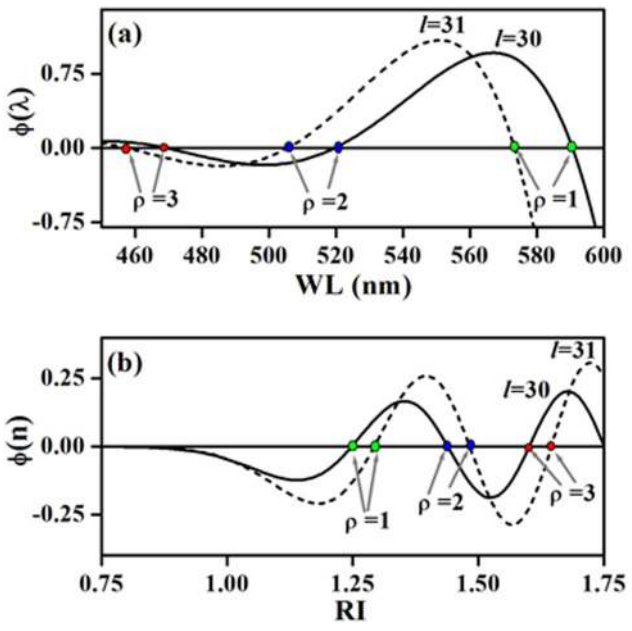

FIG. 5. (a) ϕ_l as a function of λ for $l = 30$ (solid line) and $l = 31$ (dashed line) for fixed $n = 1.5$ and $a = 2.2\,\mu$m; (b) ϕ_l as a function of n for $l = 30$ (solid line) and $l = 31$ (dashed line), for $a = 2.2\,\mu$m and $\lambda = 0.5\,\mu$m. Green, blue, and red spots indicate the modes corresponding to $\rho = 1$, 2, and 3, respectively, which are also indicated by arrows. No solution exists in the region $n < 1$.

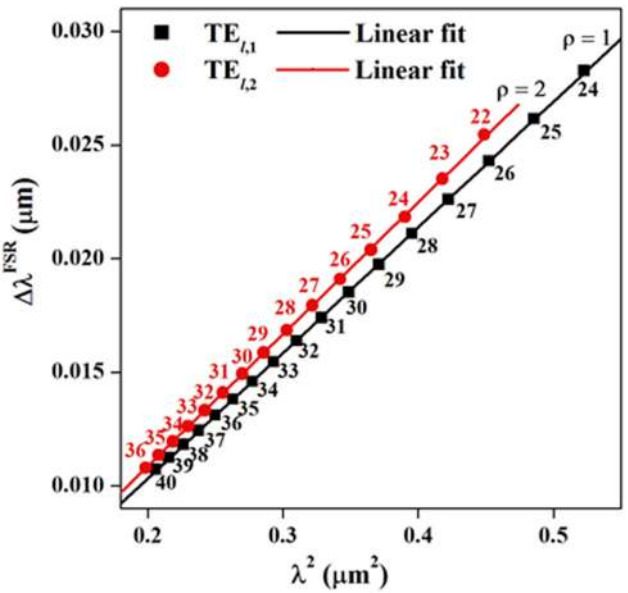

FIG. 6. $\Delta\lambda^{FSR}$ as a function of λ^2 for a Mie sphere with $a = 2.2\,\mu$m and $n = 1.5$. Modes with $\rho = 1$ and $\rho = 2$ are denoted by black squares and red spheres, respectively. Value of l is indicated near the mode position.

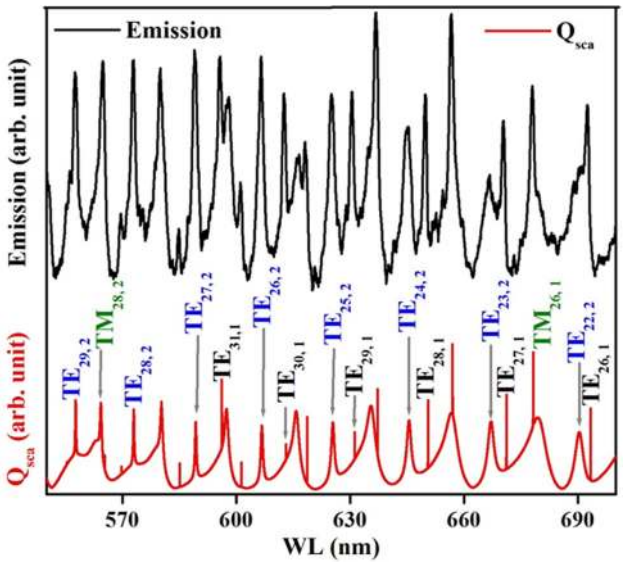

FIG. 7. MDR modes on the micro PL spectrum of a single sphere (4.32 μm) are shown by the black curve (upper plot). The corresponding scattering efficiency spectrum obtained using Mie theory with the corrected RI is shown by the red curve (lower plot), for a smaller range. Identification of the TE modes with $\rho = 1$ and $\rho = 2$ is presented over the corresponding peak of the Mie plot. To avoid cluttering, only two TM modes with the lowest value of l corresponding to $\rho = 1$ and highest value of l corresponding to $\rho = 2$ are included in the region of interest.

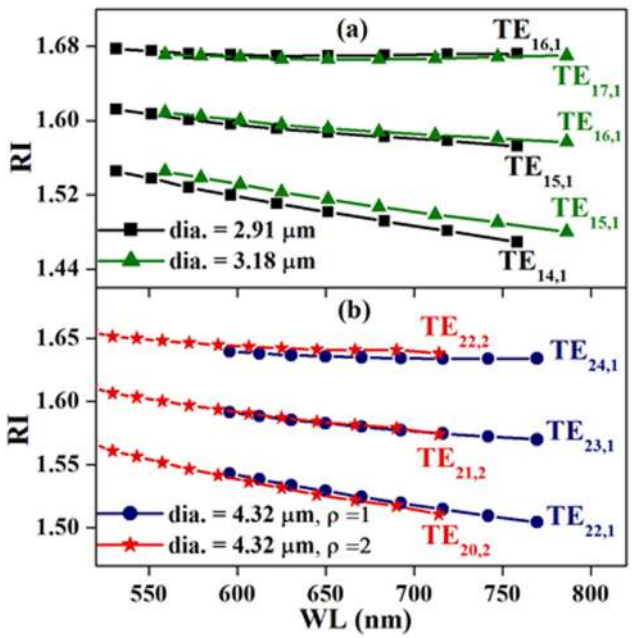

FIG. 8. RI as a function of WL for different assignment of mode numbers: (a) for spheres with smaller diameters: 2.91 μm (indicated by black squares) and 3.18 μm (indicated by green triangles); (b) with larger diameter 4.32 μm, where calculations for $\rho = 1$ and $\rho = 2$ modes are indicated by blue circles and red stars, respectively.

approximation of RI (n_l^1) obtained using Eq. (6), which can be derived from Eq. (1).

$$n_l^1 = 1/\Delta x_l. \tag{6}$$

Only TE modes with $\rho = 1$ are used for the first approximation. TE modes are chosen as they appeared more distinguishable compared to TM modes in the experimental MDR spectrum. For the first guess of l, RI is considered to be constant and equal to the average of n_l^1 for the entire range of consideration. With this RI and the radius of the sphere obtained from SEM image, a set of $[l^1_{\min,\rho}, l^1_{\max,\rho}]$ is obtained in the spectral region of observation. $l^1_{\min,\rho}$ and $l^1_{\max,\rho}$ are the minimum and maximum mode numbers corresponding to mode positions with maximum and minimum WL value in the range of observation, respectively. The $\rho = 1$ and $\rho = 2$ modes appearing in this region are grouped separately. However, spectral position of the modes obtained with this approximation do not match with that of experimental spectrum because (i) being obtained from zeroth order approximation, Eq. (6) is not suitable enough to define modes with lower l and higher ρ, and (ii) Eq. (6) is obtained neglecting RI dispersion. We proceed to assign $l^{\exp}_{1,\rho} = l^1_{\min,\rho}$ and so on, to calculate the set of RI, $[n^{\exp}_{\min,\rho}, n^{\exp}_{\max,\rho}]$ corresponding to each mode position using Eq. (4), from the size of the sphere and the set of spectral mode positions $[\lambda^{\exp}_{l_1,\rho}, \lambda^{\exp}_{l_N,\rho}]$. $l^{\exp}_{1,\rho}$ corresponds to the mode number of the highest value of WL ($\lambda^{\exp}_{l_1,\rho}$), in the experimental MDR spectrum, for a particular value of ρ. RI for $\rho = 1$ and $\rho = 2$ modes are the first and second solutions of Eq. (4), respectively, obtained numerically using MATLAB codes. At the end of this step, we have an estimate of RI and its dispersion. Estimation of the RI would be correct when mode numbers are assigned correctly.

To deal with the dispersion produced by the mesoporous sphere, we examine the chromatic dispersion of bulk anatase TiO_2. We find that the dispersion characteristics of the bulk RI of anatase TiO_2 in the region of interest[28] follow the Sellmeier equation with one resonance term as given in Eq. (7).

$$n^2 = 1 + \frac{p_1\lambda^2}{\lambda^2 - p_2}, \tag{7}$$

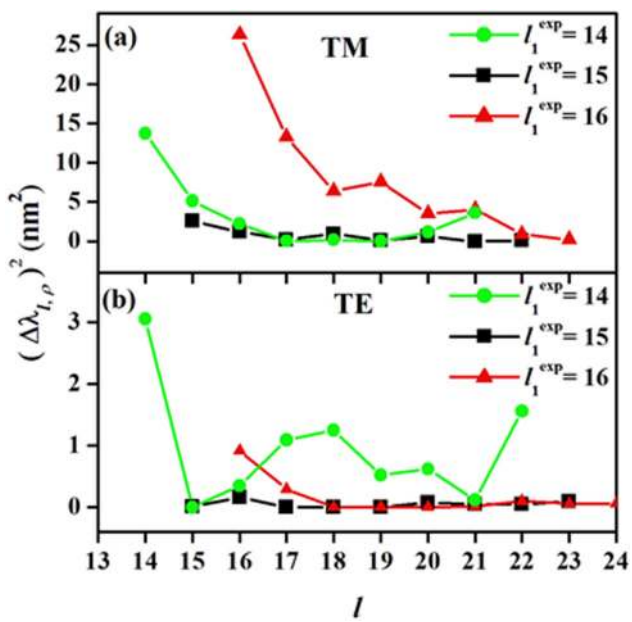

FIG. 9. $(\Delta\lambda_{l,\rho})^2$ vs l plotted for 2.91 μm sphere when the smallest mode was assigned the values: $l^{\exp}_{1,\rho=1} = 14$ (green spheres), 15 (black squares), and 16 (red triangles) for (a) TM and (b) TE modes.

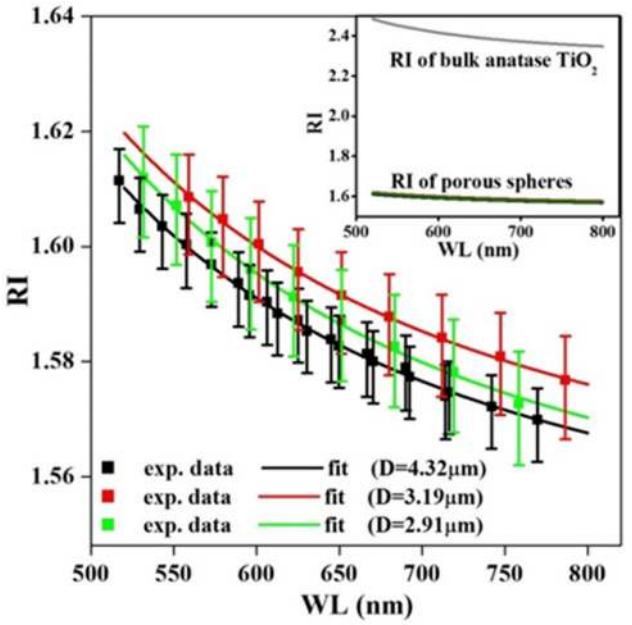

FIG. 10. The Sellmeier equation fitted for the data obtained from experimental emission spectrum for spheres with diameter 4.32 μm, 3.18 μm, and 2.91 μm indicated in black, red, and green, respectively. RI dispersion for bulk anatase TiO_2 (gray line) and that of the porous spheres are shown in the inset.

where p_1 and p_2 are the Sellmeier coefficients. As it seems reasonable to expect porous TiO_2 spheres also to be defined by similar dispersion relation, the sets of $[n^{\exp}_{\min,\rho}, n^{\exp}_{\max,\rho}]$ and $[\lambda^{\exp}_{l_1,\rho}, \lambda^{\exp}_{l_N,\rho}]$ for both $\rho = 1$ and $\rho = 2$ modes of the porous TiO_2 spheres have been fitted with the Sellmeier equation using Eq. (7). It is not surprising to note that the presence of high porosity leads to significant changes in the Sellmeier coefficients.

Estimation of the RI and its associated dispersion would be correct when mode numbers are assigned correctly. Though only TE modes have been considered for this assignment, it is found that the corrected RI and the associated dispersion leads to the observed TM mode positions as well, indicating the consistency of the procedure adopted. We further expect that the simulated scattering spectrum of the effectively isotropic sphere, computed using MiePlot,[30] matches the observed spectrum if the estimated RI and the associated dispersion is correct. Therefore, we demand that for the correct assignment of mode numbers, the mean square difference between experimental and simulated mode positions ($\langle(\Delta\lambda_{l,\rho})^2\rangle$) as given in Eq. (8) should be a minimum for all distinguishable TE and TM modes.

$$\langle(\Delta\lambda_{l,\rho})^2\rangle = \langle(\lambda^{\exp}_{l,\rho} - \lambda^{Mie}_{l,\rho})^2\rangle. \tag{8}$$

$\lambda^{\exp}_{l,\rho}$ and $\lambda^{Mie}_{l,\rho}$ in Eq. (8) indicate mode positions of the experimental PL spectrum and simulated Mie spectrum, respectively.

For the next step in the estimation of RI, the set $[l^{\exp}_{1,\rho}, l^{\exp}_{N,\rho}]$ is assigned to shifted values of the approximate set $[l^{1}_{\min,\rho}, l^{1}_{\max,\rho}]$, shifting by ±1 steps, with RI as a function of WL calculated for each trial shift as shown in Fig. 11 of Appendix A. In each trial, mode positions and hence $\langle(\Delta\lambda_{l,\rho})^2\rangle$ are calculated for all the distinguishable TE and TM modes. Amongst all the assignments of mode numbers to the set $[l^{\exp}_{1,\rho}, l^{\exp}_{N,\rho}]$, the set of RI corresponding to the assignments with minimum $\langle(\Delta\lambda_{l,\rho})^2\rangle$ is considered to be the correct.

Geometric dispersion occurs due to the dependence of Δx^{FSR}_l on l, and it increases as the value of l decreases. Chromatic dispersion occurs due to the dispersion in the RI of the material. The proposed method is capable of extracting the RI with or without chromatic dispersion up to the third decimal place with numerical dispersion limiting the precision to the fourth decimal place. Details of the numerical dispersion entailed in the proposed scheme are in Appendix A.

B. Analysis of the experimentally obtained MDR modes

1. Mode identification

The MDR modes are observed above the photoluminescence envelope of the emission spectrum in Fig. 4(a). Modes are labeled as $TE_{l,\rho}$ (or $TM_{l,\rho}$). Spectral densities of the modes are observed to decrease as the size of the sphere decreases. The efficiency spectrum simulated with Mie theory is modulated by a slowly varying pattern caused by the interference of the incident and forward scattered light.[22] As this slowly varying pattern is not relevant in the present context, it is not considered further. Mode identification for the 4.32 μm sphere, after removing the envelopes from the emission and scattering efficiency spectra, can be seen in Fig. 7. Both $\rho = 1$ as well as $\rho = 2$ modes seem to agree well with simulated scattering efficiency spectrum. The $\rho = 1$ mode is observed to decay with decreasing WL, while the $\rho = 2$ mode becomes more distinguishable in the region of lower WL. The mode positions of the experimental and simulated MDR spectra for all the three spheres are given in Tables III and IV of Appendix B.

2. Refractive index correction for porous TiO_2 sphere

In the MDR spectrum of spheres with smaller diameters (2.91 μm and 3.12 μm) shown in Fig. 4(a), the $\rho = 2$ mode is not distinguishable enough. In this case, only the $\rho = 1$ mode is considered for RI extraction. It is observed that $\langle(\Delta\lambda_{l,\rho})^2\rangle$ is minimum for the assignment of the largest values of $l^{\exp}_{i,\rho}$ ($i = 1, 2, \ldots$), for which calculated RI vs WL has a negative slope and hence can be fitted with the Sellmeier equation given in Eq. (7). As shown in Fig. 8(a), the dispersion obtained for $l^{\exp}_{1,\rho=1} = 16$ and 17 (or higher values) corresponding to the spheres with diameter 2.91 μm (indicated in black) and 3.18 μm (indicated in green), respectively, cannot be fitted well with Eq. (7). However, it is found that for $l^{\exp}_{1,\rho=1} =$ 15 and 16, the dispersion can be fitted with Eq. (7), and $\langle(\Delta\lambda_{l,\rho})^2\rangle$ tends to a minimum for the spheres with diameters 2.91 μm and 3.18 μm, respectively. Figure 9 quantifies how $(\Delta\lambda_{l,\rho})^2$ responds to the choice of l for the sphere of diameter 2.91 μm. The values of $(\Delta\lambda_{l,\rho})^2$ are larger for TM (TE), when $l^{\exp}_{1,\rho=1} = 16$ (14). However, it can be observed that when $l^{\exp}_{1,\rho=1} = 15$, the values of $(\Delta\lambda_{l,\rho})^2$ remain nearly constant, and $\langle(\Delta\lambda_{l,\rho})^2\rangle$ is a minimum for both TE and TM modes.

In the case of the sphere with larger diameter (4.32 μm), the $\rho = 2$ mode is more distinguishable in the lower WL region. It can be observed in Fig. 8(b) that the dispersion

TABLE I. Sellmeier coefficients for bulk anatase and porous sphere (PS).

Sample	p_1	p_2 (μm)	R^2
Bulk	4.108	0.05490	0.998
PS dia. = 4.32 μm	1.372	0.03746	0.998
PS dia. = 3.18 μm	1.396	0.03790	0.999
PS dia. = 2.91 μm	1.375	0.03962	0.998

corresponding to $\rho = 1$ and $\rho = 2$ modes are separate curves when $l^{\text{exp}}_{1,\rho=1} = 22$ (24) and $l^{\text{exp}}_{1,\rho=2} = 20$ (22). However when $l^{\text{exp}}_{1,\rho=1} = 23$ and $l^{\text{exp}}_{1,\rho=2} = 21$, it is observed that corresponding dispersion curves nearly merge and can be fitted using Eq. (7) by a single dispersion curve. In this case, $\langle(\Delta\lambda_{l,\rho})^2\rangle$ is observed to be a minimum.

The Sellmeier equation fitted for the MDR modes in emission spectra is presented in Fig. 10. RI dispersion of the sphere compared to that of the bulk anatase TiO_2[28] is shown in the inset of Fig. 10. RI of the spheres can be seen to be much less than that of bulk. There is a probable error in the refractive index due to an error in particle size. To estimate this error, the SEM image is used to extract 10 diameters of the sphere along 10 different orientations. The error bars in Fig. 10 indicate the spread of refractive index due to the spread of the diameters estimated along different orientations. It may be noted that changes in RI can occur up to the second significant digit. The slight differences between the dispersion curves related to different spheres may be due to slight differences in the pore distribution and the pore volume fraction in the interior of the sphere.

The clear variation in the RI at the third decimal position, observed in two neighboring modes, is considered to arise from the chromatic dispersion. As discussed in Appendix A, numerical dispersion manifesting in the fourth decimal position sets the limits to the evaluating scheme particularly while dealing with the modes having smaller values of l. The values of Sellmeier coefficients of the RI dispersion and the regression coefficient (R^2) obtained from the fitting for bulk TiO_2 and for porous microspheres are shown in Table I.

3. Analysis of the Quality factor

For an ideal homogeneous, isotropic, and non-absorbing sphere, the Q-factor is determined only by radiative losses and is denoted by Q_{rad}. Higher values of Q_{rad} occur for the modes with higher l and lower ρ. For a particular value of ρ, Q_{rad} increases and tends to infinity with increasing l. However, such a trend is not to be expected in the experimental spectrum of a mesoporous sphere. The total Q-factor of an MDR mode for a non-ideal case can be governed by various processes as given in Eq. (9).

$$\frac{1}{Q_{total}} = \frac{1}{Q_{rad}} + \frac{1}{Q_{other}}, \tag{9}$$

with Q_{other} in turn written as Eq. (10):

$$\frac{1}{Q_{other}} = \frac{1}{Q_{mat}} + \frac{1}{Q_{surf}} + \frac{1}{Q_{con}}, \tag{10}$$

where, Q_{mat}, Q_{surf}, and Q_{con} are the Q-factors related to the losses caused by absorption by the intrinsic material, scattering due to surface inhomogeneities, and contacts of the resonator with external agents, respectively.[31]

Q-factors of the observed modes are of the order of 10^2, which is much less than that of an equivalent isotropic homogeneous loss-less sphere due to various sources of losses indicated in Eq. (10). It is surmised that Q_{surf} may have a significant contribution due to the porous structure of the sphere. Furthermore, Q_{mat} appears to exist due to the presence of impure elements (N and C) as well as oxygen vacancies. The Q-factors of the $\rho = 1$ mode for the smaller spheres (of diameters 3.18 μm and 2.91 μm) of Fig. 4(a) do not decay over the spectrum considered. However, for the larger sphere of diameter 4.32 μm, the Q-factors for the $\rho = 1$ modes start decaying toward the lower WL region as shown in Fig. 4(a) as well as in Fig. 7 (experimental MDR spectrum). However, the $\rho = 2$ mode does not seem to decay as much. Equation (9) implies that the value of Q_{total} is lower than the lowest of Q_{rad} and Q_{other}. When Q_{other} is much lower than Q_{rad}, Q_{total}:Q_{rad} ratio is much lower for the modes with higher l and lower ρ, or in other words, for the modes with higher value of Q_{rad}.

IV. SUMMARY AND CONCLUSION

Mesoporous TiO_2 spheres of high surface area, consisting of nano-crystalline grains of average size 7 nm (from XRD data) and pores of size about 7.6 nm (from BJH estimation), supporting MDR modes have been synthesized. Though the bulk anatase phase of TiO_2 is a birefringent material, the mesoporous sphere is found to behave as an effective isotropic medium as it is made up of nanocrystalline grains with random crystallographic orientations and pores, both of which are very small compared to the WL of the light inside the sphere. RI of the mesoporous TiO_2 medium and the associated chromatic dispersion is determined using an iterated determination of l by minimizing the WL difference between computed spectral position and observed spectral position. The suggested procedure for the estimation of RI and its dispersion works with either TE or TM modes or with both, deals with higher order radial modes as long as $1 << x < l$ is satisfied, provides the best estimates within a few iterations, and does not require bulk phase values. The numerical dispersion estimated in the current implementation limits the estimation of chromatic dispersion to the third significant digit.

Due to the high porosity, effective RI of the mesoporous sphere decreases significantly from its bulk value. The presence of high pore volume fraction is found to change the dispersion of refractive index as well from that of the bulk. FSR of a spherical resonator is related to the size and RI of the sphere. A lower refractive index leads to a lower confinement of the MDR modes and hence higher FSR. Reduction in the RI value due to porosity can be compensated by increasing the size of the sphere to maintain the required FSR.

Most of the applications such as photo-catalysis reaction, energy conversion and transfer, water splitting, etc. require TiO_2 to have high scattering efficiency. Enhancement of the surface area of mesoporous TiO_2 sphere facilitates interaction

with external molecules and atoms, making it suitable for various applications. The presence of MDR mode helps enhance the scattering efficiency and hence the performance of the sphere. TiO_2 microspheres with MDR modes as well as high surface area would be a very promising optical material particularly in the applications related to photocatalysis.

APPENDIX A: ESTIMATION OF NUMERICAL DISPERSION IN RI EXTRACTION

Calculations of RI using the proposed procedure for the MDR spectra obtained by MiePlot[30] can be seen in Fig. 11. MiePlot is used to obtain the MDR spectra of a sphere of radius 1.5 μm and a constant RI 1.5. By assigning different mode numbers to the spectral positions, RI is estimated using Eq. (4). In the first approximation, RI from FSR, using Eq. (6), was found to be 1.3701. In the range of 500–800 nm, the value of lowest angular mode number (l_1) obtained solving Eq. (4) with this RI is 13. For $l_1 < 15$, computed RI is observed to increase with l. For $l_1 > 15$, it is observed to decrease with l. For $l_1 = 15$, RI was observed to be nearly constant at 1.5 with slight deviation at the fourth decimal point. This deviation was observed to be more for lower values of l as shown in Table II. Modes with smaller l values in the scattering efficiency spectrum are affected by contributions from other neighboring modes. The proposed method for RI determination would be more precise when applied to modes with larger values of l ($l >> 1$).

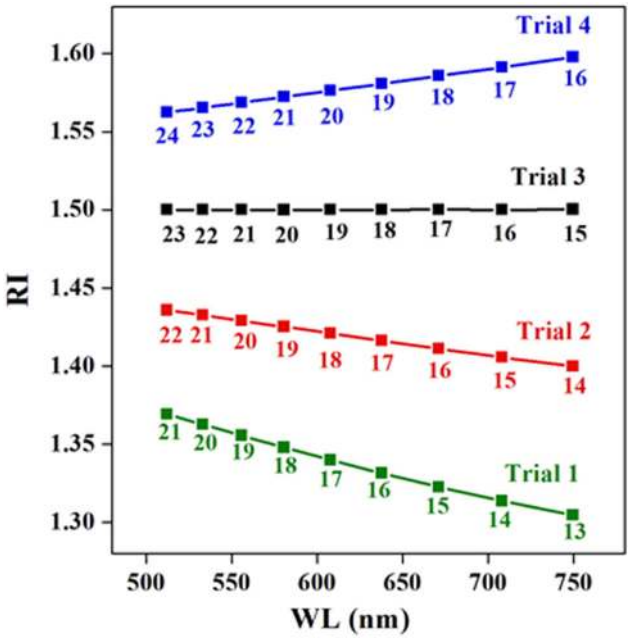

FIG. 11. Computed RI using mode positions obtained by MiePlot[30] for a sphere of radius 1.5 μm and a constant RI 1.5 for different assignments of angular mode numbers. The four trials show RI computations with initial angular momentum mode number, $l_1 = 13$, 14, 15, and 16 respectively for TE polarization with first radial mode number.

TABLE II. Computed RI for trial 3 in Fig. 11.

l	20	19	18	17	16	15	14
RI	1.4999	1.5	1.5	1.5001	1.5	1.5002	1.5003

APPENDIX B: MODE POSITIONS OF EXPERIMENTAL AND SIMULATED DATA

The resonance positions of experimental and simulated scattering spectra are given in Tables III and IV.

As described in Sec. III B 2, the square of the difference between measured and computed spectral positions, taken from these tables, tends to a minimum for the correct choice of l.

TABLE III. Experimental and simulated mode positions obtained from PL spectra and Mie calculation, respectively, for spheres with diameter 2.91 μm and 3.18 μm.

l	Sphere diameter = 2.91 μm				Sphere diameter = 3.18 μm			
	$TE_{l,1}$		$TM_{l,1}$		$TE_{l,1}$		$TM_{l,1}$	
	$\lambda_{l,1}^{exp}$ (nm)	$\lambda_{l,1}^{Mie}$ (nm)	$\lambda_{l,1}^{exp}$ (nm)	$\lambda_{l,1}^{Mie}$ (nm)	$\lambda_{l,1}^{exp}$ (nm)	$\lambda_{l,1}^{Mie}$ (nm)	$\lambda_{l,1}^{exp}$ (nm)	$\lambda_{l,1}^{Mie}$ (nm)
15	758.34	759.2	736.65	735.19	…	…	…	…
16	718.89	719	698.05	697.1	786.35	785.98	762.94	761.9
17	683.26	683.28	663.99	663.24	747.27	746.65	725.92	724.61
18	651.31	651.32	633.48	632.92	711.83	711.43	692.32	691.2
19	622.43	622.57	606.08	605.61	680.02	679.72	661.9	661.09
20	596.41	596.57	581.31	580.93	651.21	651.02	634.47	633.82
21	572.69	572.97	558.7	558.47	625.03	624.92	609.64	609
22	551.52	551.42	538.14	538	601.39	601.1	586.93	586.32
23	531.57	531.71	…	…	579.46	579.26	566.04	565.52
24	…	…	…	…	559.09	559.17	547.06	546.37

TABLE IV. Experimental and simulated mode positions obtained from PL spectra and Mie calculation respectively for spheres with diameter 4.32 μm.

l	$TE_{l,1}$		$TM_{l,1}$		$TE_{l,2}$	
	$\lambda_{l,1}^{exp}$ (nm)	$\lambda_{l,1}^{Mie}$ (nm)	$\lambda_{l,1}^{exp}$ (nm)	$\lambda_{l,1}^{Mie}$ (nm)	$\lambda_{l,2}^{exp}$ (nm)	$\lambda_{l,2}^{Mie}$ (nm)
21	…	…	…	…	714.01	715.4
22	…	…	780.87	781.28	689.96	690.3
23	769.57	770.83	752.09	752.37	666.6	667.06
24	741.8	742.95	725.36	725.72	644.96	645.48
25	716.16	717.19	700.7	701.08	625.08	625.41
26	692.42	693.31	677.95	678.23	606.44	606.71
27	670.32	671.13	656.41	656.97	589.05	589.25
28	649.74	650.47	636.79	637.15	572.77	572.93
29	630.42	631.17	618.18	618.63	557.48	557.62
30	612.51	613.11	601.18	601.28	543.07	543.26
31	595.66	596.18	584.75	585	529.37	528.842
32	579.9	580.27	569.54	569.69	…	…

[1]R. K. Chang and A. J. Campillo, *Optical Processes in Microcavities* (World Scientific, Singapore, 1996).
[2]J. Ward and O. Benson, Laser Photon. Rev. **5**, 553–570 (2011).
[3]M. R. Foreman, J. D. Swaim, and F. Vollmer, Adv. Opt. Photonics **7**, 168–240 (2015).
[4]G. Lin, A. Coillet, and Y. K. Chembo, Adv. Opt. Photonics **9**, 828–888 (2018).
[5]J. Park, S. K. Ozdemir, F. Monifi, T. Chadha, S. He Huang, P. Biswas, and L. Yang, Adv. Opt. Mater. **2**, 711–717 (2014).
[6]A. Paunoiu, R. S. Moirangthem, and A. Erbe, Phys. Status Solidi RRL **9**, 241–244 (2015).

[7]M.-C. Tsai, T.-L. Tsai, D.-B. Shieh, H.-T. Chiu, and C.-Y. Lee, Anal. Chem. **81**, 7590–7596 (2009).
[8]T. K. Das, P. Ilaiyaraja, and C. Sudakar, ACS Appl. Energy Mater. **1**, 765–774 (2018).
[9]M. Pelaez, N. T. Nolanb, S. C. Pillai, M. K. Seeryc, P. Falaras, A. G. Kontos, P. S. M. Dunlope, J. W. J. Hamiltone, J. A. Byrne, K. O'Shea, M. H. Entezari, and D. D. Dionysioua, Appl. Catal. B **125**, 331–349 (2012).
[10]T. H. B. Ngo, C. H. Chien, S. H. Wu, and Y. C. Chang, Opt. Express **24**, 16010–16015 (2016).
[11]H. Ikari, K. Okanishi, M. Tomita, and T. Ishidate, Opt. Mater. **30**, 1323–1326 (2008).
[12]R. S. Moirangthem, P.-J. Cheng, P. Ching-Hang Chien, B. Trong, H. Ngo, S.-W. Chang, C.-H. Tien, and Y.-C. Chang, Opt. Express **21**, 3010–3020 (2013).
[13]L. Cao, D. Chen, and R. A. Caruso, Angew. Chem. Int. Ed. **52**, 10986–10991 (2013).
[14]D. Chen, L. Cao, F. Huang, P. Imperia, Y. B. Cheng, and R. A. Caruso, J. Am. Chem. Soc. **132**, 4438–4444 (2010).
[15]M. C. Mathpal, A. K. Tripathi, M. K. Singh, S. P. Gairola, S. N. Pandey, and A. Agarwal, Chem. Phys. Lett. **555**, 182–186 (2013).
[16]Z. A. ALOthman, Materials **5**, 2874–2902 (2012).
[17]J. Shi, J. Chen, Z. Feng, T. Chen, Y. Lian, X. Wang, and C. Li, J. Phys. Chem. C **111**, 693–699 (2007).
[18]C. Jin, B. Liu, Z. Lei, and J. Sun, Nanoscale Res. Lett. **10**, 95 (2015).
[19]C. M. Liu, X. P. Li, and X. T. Zu, Chin. J. Phys. **47**, 207–214 (2009); available at http://www.airitilibrary.com/Publication/alDetailedMesh?DocID=05779073-200904-47-2-207-214-a.
[20]Y. Nakano, T. Morikawa, T. Ohwaki, and Y. Taga, Appl. Phys. Lett. **87**, 052111 (2005).
[21]I. Kalyan and C. V. Krishnamurthy, Int. J. Res. Eng. Technol. **6**, 18–22 (2017).
[22]C. F. Bohren and D. R. Huffman, *Absorption and Scattering of Light by Small Particles* (Wiley Interscience Publication, New York, 1998).
[23]M. I. Tribelsky and A. E. Miroshnichenko, Phys. Rev. A **93**, 053837 (2016).
[24]C. C. Lam, P. T. Leung, and K. Young, J. Opt. Soc. Am. B **9**, 1585–1592 (1992).
[25]C. Swindal, D. H. Leach, R. K. Chang, and K. Young, Optics Lett. **18**, 191–193 (1993).
[26]P.-t. Leung, S.-w. Ng, K.-m. Pang and K.-m. Lee, Optics Lett. **27**, 1749–1751 (2002).
[27]M. Ornigotti and A. Aiello, Phys. Rev. A **84**, 013828 (2011).
[28]G. E. Jellison Jr., L. A. Boatner, J. D. Budai, B. S. Jeong, and D. P. Norton, J. Appl. Phys. **93**, 9537–9541 (2003).
[29]S. Auvinen, M. Alatalo, H. Haario, E. Vartiainen, J. P. Jalava, and R. J. Lamminmaki, J. Phys. Chem. C **117**, 3503–3512 (2013).
[30]P. Laven, Appl. Opt. **42**, 436–444 (2003).
[31]M. L. Gorodetsky, A. A. Savchenkov, and V. S. Ilchenko, Optics Lett. **21**, 453–455 (1996).